Mon. Not. R. Astron. Soc. 000, 1–?? (2002) Printed 10 December 2002 (MN LATEX style file v1.4)

The Component Star Masses in RW Tri

T. Poole,[1*] K. O. Mason,[1] G. Ramsay,[1] J. E. Drew[2], R. C. Smith[3]
[1] Mullard Space Science Laboratory, University College London, Holmbury St. Mary, Dorking, Surrey RH5 6NT
[2] Imperial College of Science, Technology & Medicine, Blackett Laboratory, Prince Consort Road, London SW7 2BW
[3] Astronomy Centre, School of Chemistry Physics and Environmental Science, University of Sussex, Brighton, BN1 9QJ

in accepted form 2002 November 27

ABSTRACT
We use time-resolved spectra of the cataclysmic variable RW Tri in the I and K-band to determine the orbital velocity of the secondary star using skew mapping and cross correlation techniques respectively. We find radial velocity amplitudes of 250 ± 47 km/s in the I-band, and 221 ± 29 km/s in the K-band. We also determine the rotational velocity of the secondary star using the K-band data and find a $V_{rot} \sin i$ of 120 ± 20km/s. A combination of these results coupled with an estimate of the effect of heating on the secondary star suggests a mass ratio M_2/M_1 in the range $0.6 - 1.1$; the mass ratio range with no correction for heating is $0.5 - 0.8$. These lead to most likely estimates of the primary and secondary star masses in the range $0.4 - 0.7M_{\odot}$ and $0.3 - 0.4M_{\odot}$ respectively. Further refinement of the stellar masses is hampered by uncertain knowledge of the white dwarf orbital velocity, and we discuss evidence that at least some estimates of the white dwarf velocity are contaminated by non-orbital components.

Key words: techniques: radial velocities – binaries: eclipsing – stars: individual: RW Tri – novae, cataclysmic variables – infrared: stars.

1 INTRODUCTION

RW Tri is an eclipsing nova-like cataclysmic variable (CV) system with an orbital period of 5 hours 34 mins. Nova-like systems contain a non-magnetic white dwarf primary and a late type (K-M) secondary star that fills its Roche lobe, transferring mass to the white dwarf via an accretion disc.

Since first being observed as an eclipsing variable (Protitch 1937) multi-wavelength studies of RW Tri have provided much insight into the system, but have yet to yield an accurate measurement of the masses of the two component stars. By observing the velocities of the component stars, their masses can be calculated using Kepler's laws. A number of authors have attempted to measure the radial velocity of the white dwarf (e.g. Kaitchuck *et al.* 1983, Still *et al.* 1995 and Mason *et al.* 2002), but thus far little work has been done on the secondary star.

Measurement of the secondary star velocity is hampered by the large contrast in optical brightness between it and the accretion disk. Weak secondary star absorption features were detected in the I-band spectrum of RW Tri by Friend *et al.* (1988), and later used by Smith *et al.* (1993) to estimate the secondary star velocity as $\sim$ 250km/s using a 'skew-mapping' technique (cf. Smith *et al.* 1998a). Dhillon *et al.* (2000) have detected secondary star features in low-resolution K-band spectra of RW Tri. The relative contribution of the secondary star is higher in the K-band and the equivalent width of the absorption features greater as a consequence.

In this paper we report phase-resolved spectral observations of RW Tri in the K-band, covering the binary orbit. We use these observations to determine the radial velocity of the secondary star in RW Tri. We also re-analyse the original I-band spectra of Smith *et al.* (1993). Based on these results we revisit the mass ratio and the masses of the component stars in RW Tri and discuss their implications.

2 I-BAND DATA

We have re-analysed the RW Tri near I-band data of Smith *et al.* (1993) using the back-projection routines in the software package MOLLY written by Tom Marsh (see also Vande Putte *et al.* 2002), combined with a Monte Carlo error analysis. We use the method of 'skew-mapping' (Smith *et al.* 1993) in which the orbital phase-resolved data are corrected for a trial orbital velocity amplitude and phase, and compared to the spectrum of a standard 'template' star. The degree of correlation between the summed corrected spectrum and the template is computed for a grid of veloc-

* tsp@mssl.ucl.ac.uk

Table 1. Template stars from Martin (1988).

Name	Color Index	Spectral type
Gl 653	0.49	K5
Gl 717	0.54	K7
Gl 673	0.60	K7
Gl 488	0.67	M0-
Gl 383	0.70	M0
Gl 281	0.71	M0
Gl 908	0.87	M1.5

ity amplitudes and phases to produce the skew map. This method is useful when the spectral features of the secondary are too weak to produce significant cross correlation peaks using individual spectra.

The I-band spectra were obtained using the Isaac Newton Telescope (INT) on La Palma, and the 831R grating, giving a wavelength coverage of 7700Å - 8300Å. This range includes the Na I absorption doublet feature (λ8183.3Å, λ8194.8Å) that is expected in the spectrum of a late-type star. A total of 27 spectra were taken over two nights spanning the full orbital cycle: 19 spectra were taken on the 2^{nd} September 1985, and 8 spectra were taken on 3^{rd} September 1985. The ephemeris of Robinson *et al.* (1991) was used to phase the spectra. A range of 7 template stars of spectral type K5-M1.5 were taken from Martin (1988), the details of which are given in Table 1. Template and RW Tri spectra were normalised by dividing by a low-order spline fit to the respective continuum.

A range of skew maps with total systemic velocities (RW Tri + template) from -50km/s to 50km/s, were produced for each template. A mask between 7760Å and 7800Å was used to remove the accretion disc absorption feature of neutral oxygen at 7774Å (Friend *et al.* 1988). The skew map with the strongest peak was found using the M0 template Gl 281, with a RW Tri systemic velocity of -13 km/s and secondary velocity amplitude of 250km/s. Patterson (1984) estimated the secondary star of RW Tri to be of spectral type M0, based on the empirical zero-age main-sequence (ZAMS) mass-radius relation. Our result is also consistent with the statistical prediction of K9 $\pm$ 3 by Smith & Dhillon (1998b). The other M0 template (Gl 383 - Table 1) and the M0- template (Gl 488 - Table 1), produce skew maps with K_2 of 259 km/s and 255 km/s respectively, consistent with the result for template Gl 281.

A Monte Carlo simulation was used to calculate the error on the skew map results. The noise level on the normalised RW Tri spectra was used as a seed to generate normally-distributed random numbers that were added to the RW Tri spectra. In this way 150 skew maps were produced and the distribution of peak velocity values was measured to derive an error. Each trial was weighted with the line integral intensity of its respective map in computing the standard deviation of the resulting distribution. In this way, we determine that the best fit skew map (Figure 1) has a secondary velocity amplitude of $K_2 = 250 \pm 47$ km/s.

Vande Putte *et al.* (2002) have obtained results using the same set of RW Tri data but a different set of templates ranging from K5-M4.5. They find a best fit using the M1 template Gl 514 and $K_2 = 263 \pm 30$ km/s with a systemic velocity of -11 ± 15km/s agreeing with our results within

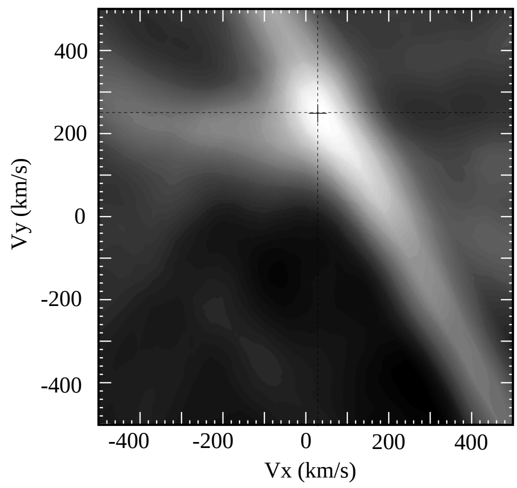

Figure 1. Best fit skew map of RW Tri with template Gl 281, with a systemic velocity of -13 km/s. The white of the grey scale represents the strongest cross correlation. The peak of 250 ± 47km/s on the map is represented by +.

error. The differences between their value of K_2 and ours (which is within the respective errors) can be ascribed to the different set of templates used, and is a measure of the systematic uncertainty.

3 K-BAND DATA

The secondary star only contributes ~10% of the flux in the I-band, compared to an estimated ~65% in the K-band (Dhillon *et al.* 2000), so we would expect to see secondary star absorption features more easily at longer wavelengths. Absorption features due to the secondary star have been observed in the K-band spectrum of RW Tri by Dhillon *et al.* (2000) at low spectral resolution, which motivated us to investigate whether we could use these features to measure the secondary star velocity directly using a standard cross correlation technique.

3.1 Observations

Observations of RW Tri were made in the K-band on the 6^{th} and 7^{th} August 2000 using CGS4 on the United Kingdom Infra-Red Telescope (UKIRT). The 150 line/mm grating gives us a spectral resolution of 100km/s at 2.2μm, and a wavelength range of 2.200μm to 2.275μm, enabling us to observe both the Na I and Ca I absorption lines recorded by Dhillon *et al.* (2000) in RW Tri. The telescope was nodded up and down the slit taking spectra at different detector positions to facilitate the removal of sky background. Summing the data from the telescope nodding positions gave a total exposure time of 600s for each RW Tri spectrum. This exposure time is equivalent to 0.03 orbital cycles which is short enough to prevent any significant smearing due to orbital effects.

A total of 35 spectra were taken of RW Tri over the two nights: 15 spectra on the first night, and 20 spectra on the second. Ten template stars in the range of spectral type K7-M2 were observed over the two nights (Table 2). Bright A-

Table 2. Template stars observed in the K-band.

Name	Spectral type	Observation date	Exposure Time (s)
Gl 397	K5	7/9/00	5
Gl 3478	K7	7/9/00	20
Gl 334	K7	6/9/00	10
Gl 182	M0	6/9/00	20
Gl 281	M0	7/9/00	12
Gl 383	M0	7/9/00	14
Gl 212	M0.5	6/9/00	10
Gl 390	M1	7/9/00	10
Gl 382	M1.5	7/9/00	7
Gl 393	M2	7/9/00	7

type stars of known broadband magnitudes and arc spectra were also observed through both nights, enabling us to flux and wavelength calibrate respectively. The bright A-stars also allowed us to remove telluric lines.

3.2 Data Reduction

Real time data reduction was undertaken at the telescope using the ORAC-DR package developed at the Joint Astronomy Centre. Bad pixels were masked and a flat field was applied to remove pixel-to-pixel variations across the array, and a bias frame was subtracted. As a result of nodding the telescope along the slit, the night sky spectrum could be accurately removed and the spectra coadded.

Bad pixels were found close to the Na I doublet feature at 22063Å and 22101Å on night 1, and 22078Å and 22116Å on night 2. The difference between the apparent wavelength of the bad pixels between the nights is due to a slight shift in the grating angle. These bad pixels were removed by interpolation.

Further data reduction was carried out using the FIGARO package. Spectra were extracted, and wavelength calibrated using the rest wavelength of arc spectra, and telluric lines were removed using the observations of A-stars. The resulting RW Tri and template spectra were flux calibrated using the A-stars, and then smoothed and rebinned on to a linear wavelength scale. The ephemeris of Robinson *et al.* (1991) was used to phase the data.

Figure 2 shows the normalised template spectra in order of spectral type. The Na I doublet and Ca I triplet absorption features can be clearly seen showing the quality of the data. There are no large differences in the depths of the Ca I and Na I lines between the different spectral types in this wavelength band, making it hard to distinguish between them. Figure 3 shows the individual spectra of RW Tri distributed in orbital phase. The Na I and Ca I absorption features appear to shift from spectrum to spectrum on each night. These features will be discussed further in Section 3.4. RW Tri was brighter on the second night. Figure 4 shows the average spectrum of RW Tri for each night with the scaled M0 template Gl 281.

3.3 The Secondary Star Velocity

The velocity of the secondary star in RW Tri was investigated by cross correlating the spectra of RW Tri with tem-

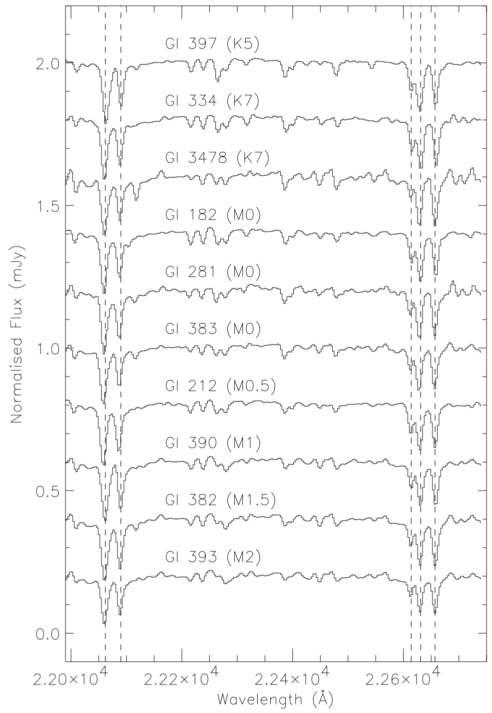

Figure 2. The normalised template spectra observed using UKIRT. The double dashed lines on the left of the plot represent the rest wavelengths of the Na I doublet λ22062Å λ22090Å and the triple dashed lines on the right represent the rest wavelengths of the Ca I triplet λ22614Å λ22631Å λ22657Å. The spectra are offset vertically by 0.2 normalised flux (mJy).

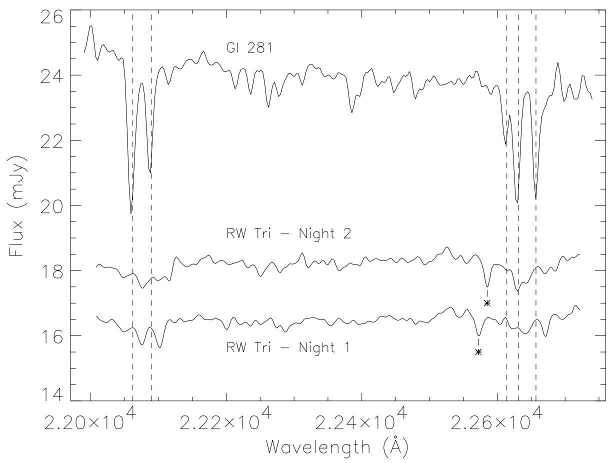

Figure 4. Average RW Tri spectra for each night. The M0 template Gl 281 is flux scaled by a factor 1/170 and offset by 1.5mJy, and the average night 2 data is offset by 1.2mJy. The absorption feature marked by $*$ is due to bad pixels. As in Figure 2 the dashed lines represent the rest wavelengths of the Na I doublet (left), and the Ca I triplet (right).

plate spectra. Both sets of spectra were normalised in the same way as described for the I-band data (Section 2), and rebinned on to the same wavelength scale. Each RW Tri spectrum was cross correlated with each template spectrum in turn. The position of the cross correlation peak was then plotted against orbital phase to produce the velocity curve of the secondary star. As in skew-mapping (Section 2), the

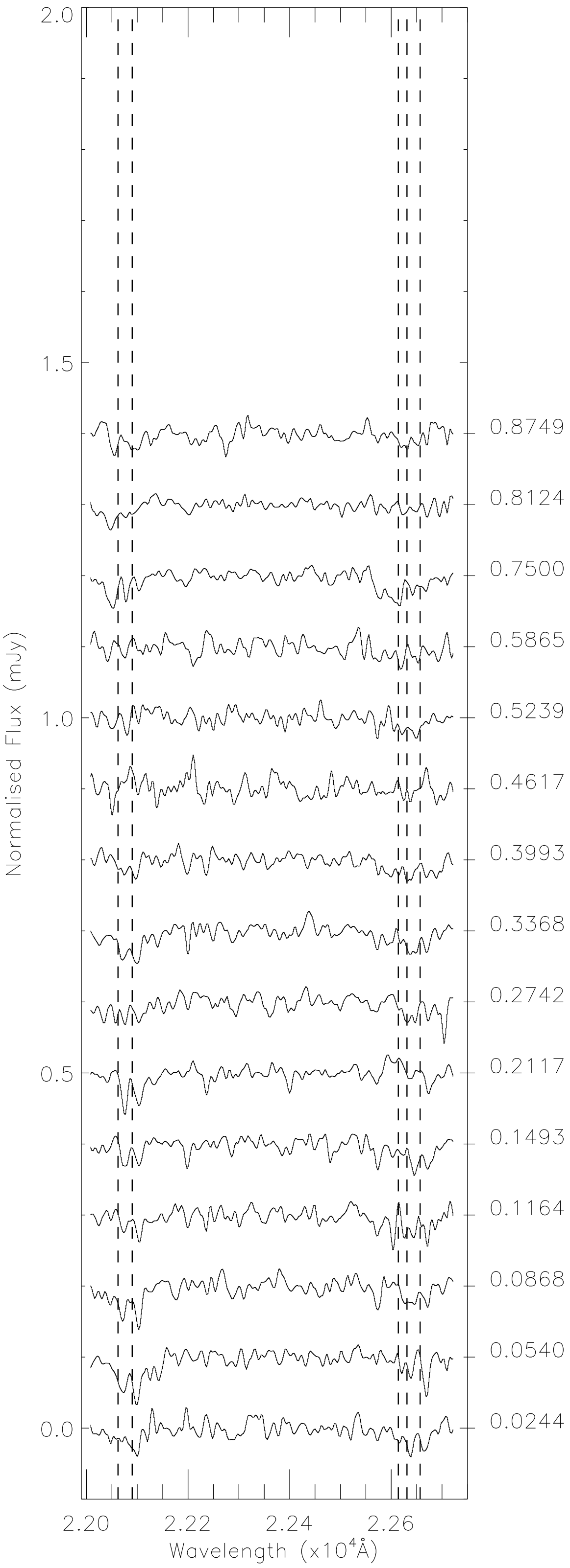

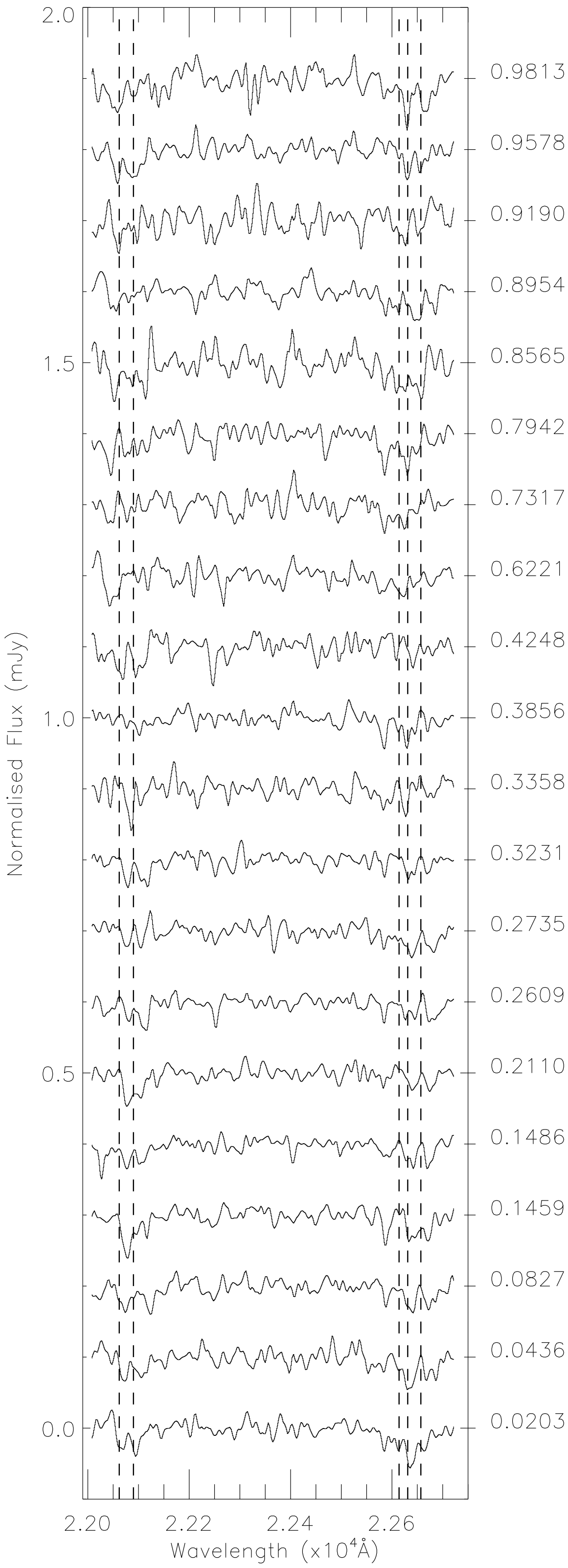

Figure 3. The left plot shows the smoothed normalised RW Tri spectra of the first night, and the right plot shows the smoothed normalised RW Tri spectra of the second night. The orbital phase is printed on the right hand side axes of both plots. The dashed lines in both plots represent the rest wavelengths of the Na I doublet (left) and Ca I triplet (right) as in Figure 2. Each spectrum is vertically offset by 0.1 normalised flux from its neighbour.

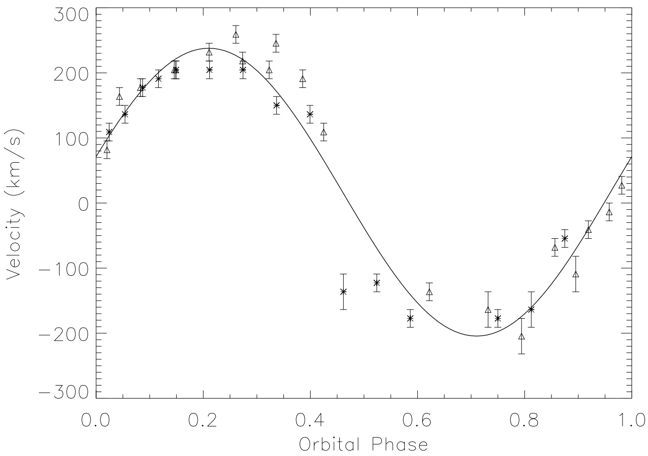

Figure 5. The best fit radial velocity curve of the two nights. The symbols $*$ and $\triangle$ represents the data points from night 1 and 2 respectively. Each point is the mean of the lags derived from the various stellar templates used (Table 2) and the error bars are the standard deviation of the results from the different templates, and therefore express the systematic error on the data due to template choice. The sinusoidal line represents the best fit velocity curve derived by least-squares fitting to the data.

spectral template that yields the strongest cross correlation peaks is the best fit to the data. All the cross correlation templates gave similar peak values, which is what we expect as there is little variation in the relative strengths of the Na I and Ca I lines over the range of late-type stars that we used (cf Figure 2). The best fit radial velocity curve of the average cross correlation lags using all the template data is illustrated in Figure 5.

This velocity curve can be parameterised as,

$$V = \gamma + K \sin(2\pi(\Phi - \Phi_o)), \tag{1}$$

where V is the radial velocity, γ is the systemic velocity, K is the orbital velocity amplitude, Φ is the binary orbital phase defined by the ephemeris of Robinson *et al.* (1991), and Φ_o is the orbital phase of blue to red zero crossing (inferior conjunction of the secondary star). A sinusoidal curve was fitted to the velocity data using the Levenberg-Marquardt algorithm in IDL; by minimising the reduced chi-squared and considering the 68.3 % (1 sigma) confidence level, a best-fit velocity and error was calculated. This gives a $K_2 = 221 \pm 29$ km/s, $\gamma = 17 \pm 20$ km/s and $\Phi_o = -0.040 \pm 0.020$ orbital phase. The results derived from individual template stars are listed in Table 3. These are all consistent within the errors, and consistent with the mean values listed above.

In Figure 6 we plot the velocity corrected average spectrum of RW Tri for each night, along with the scaled M0 template Gl 281. We can clearly see the Na I doublet and Ca I triplet in both nights. These features are broadened compared with the template spectra, due to the rotational velocity of the secondary star.

3.4 Orbital Modulation of Secondary Star Absorption Features

To search for variations in the strength of the absorption features with orbital phase, we compare the depth of the strongest features in the velocity corrected spectrum of RW Tri with the values observed in the the template star spectrum. We considered the combined regions around the Na I absorption feature (22010Å - 22140Å) and the Ca I absorption feature (22570Å - 22700Å), and mask out the rest of the spectrum. Figure 7 shows a plot of the ratio of RW Tri versus template star absorption feature deficit through the orbital cycle. There is some evidence that the secondary features are strongest near phase zero and weaker near phase 0.5. Taken at face value, this suggests that the centroid of the secondary features is shifted to the hemisphere of the secondary that faces away from the disc. Although the effect is marginal, it is in accordance with what we expect due to heating effects. The best sinusoidal fit to the data has an amplitude of 0.27 ± 0.18 (solid line in Figure 7). This sinusoidal fit to the data implies that the secondary star contributes $\sim 39\%$ of the K-band flux at phase 0.0, while at phase 0.5 this percentage is reduced to $\sim 15\%$. Hence, the absorption in the hemisphere of the secondary star nearest to the primary star is ~ 0.4 times the strength of the absorption in the hemisphere facing away from the primary.

Averaged over orbital phase these results suggest that

Table 3. Secondary star orbital parameters derived from individual template stars.

Template	K_2 (km/s)	γ (km/s)	Φ_o (orbital Phase)
Gl 397	229 ± 47	-6 ± 28	-0.044 ± 0.031
Gl 3478	218 ± 92	18 ± 65	-0.037 ± 0.068
Gl 334	218 ± 38	10 ± 27	-0.042 ± 0.027
Gl 182	217 ± 51	21 ± 36	-0.041 ± 0.037
Gl 281	223 ± 10	28 ± 6	-0.039 ± 0.007
Gl 383	220 ± 4	36 ± 3	-0.042 ± 0.003
Gl 212	219 ± 90	39 ± 64	-0.041 ± 0.064
Gl 390	221 ± 59	0 ± 37	-0.042 ± 0.037
Gl 382	222 ± 5	14 ± 8	-0.042 ± 0.008
Gl 393	217 ± 38	17 ± 27	-0.041 ± 0.026

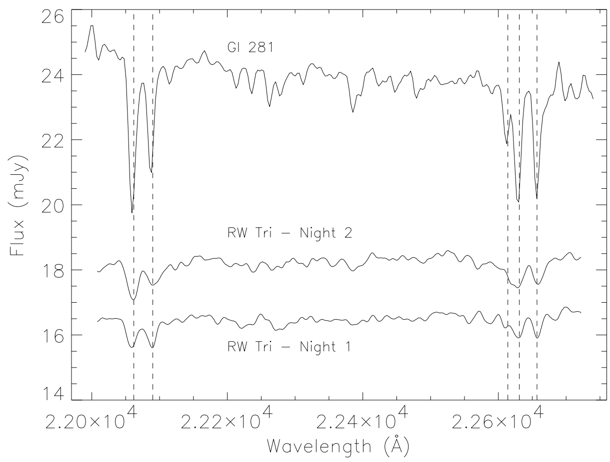

Figure 6. Velocity corrected average RW Tri spectra for each night. The M0 template Gl 281 is flux scaled by a factor 1/110 and offset by 5mJy, and the average velocity corrected night 2 data is offset by 1.2mJy. As in Figure 2 the dashed lines represent the rest wavelengths of the Na I doublet (left), and the Ca I triplet (right).

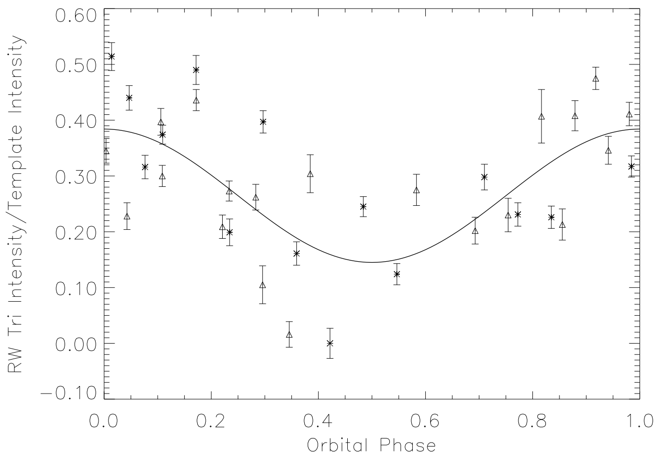

Figure 7. The total flux deficit in the Na I and Ca I RW Tri secondary star absorption features, expressed as an equivalent width, divided by the corresponding equivalent width in the template star Gl 281 (which has the highest quality spectrum among the templates measured, and is the best match to RW Tri in the I-band). We corrected for the orbital velocity shift of RW Tri in forming these numbers. Night 1 is represented by $*$, and night 2 is represented by $\triangle$. The solid line represents the best fit sinusoidal curve to the data.

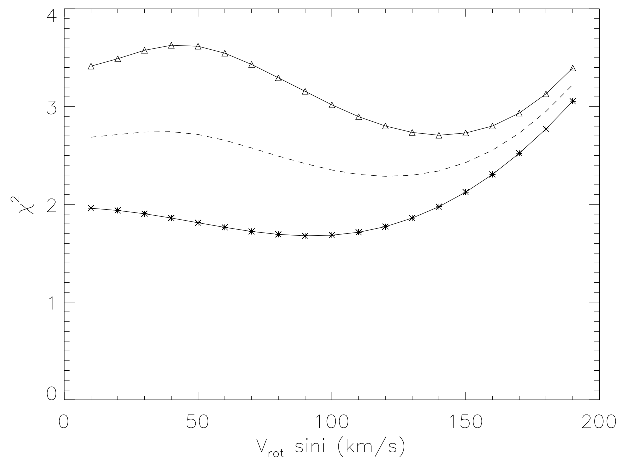

Figure 8. Plot of χ^2_ν obtained using the average of all templates after artificially broadening by $V_{rot} \sin i$ in the range $10 - 200$km/s. This shows that the minimum χ^2_ν for night 1 ($*$), night 2 ($\triangle$) and the average of the two nights night (dashed line) are 90km/s, 140km/s and 120km/s respectively.

the secondary star contributes $29 \pm 13\%$ of the K-band flux. This is considerably different from the $65 \pm 5\%$ estimated by Dhillon *et al.* (2000). The AAVSO quick look light curves of RW Tri at the time of our UKIRT observations show that RW Tri was at a magnitude of V$\sim$ 13, but during the observations of Dhillon *et al.* (2000) RW Tri appeared to be in a low state with a magnitude of ~ 13.8. Thus, RW Tri was approximately a factor of 2 brighter during our observations than when observed by Dhillon *et al.* (2000), accounting for the different estimates of the secondary star contribution. Assuming that the flux of the secondary star is constant, the accretion disc and stream in RW Tri increased by a factor of ~ 4 in brightness, between the observations of Dhillon *et al.* (2000) and ours.

3.5 Secondary Star Rotational Velocity

We noted previously that the secondary star features in RW Tri are significantly broader than in the template spectra. This is likely to be due to broadening caused by the rotation of the (phase-locked) secondary star as it orbits the white dwarf. The rotational velocity of the secondary star can be estimated by artificially broadening the template star spectrum which is assumed to have low $V_{rot} \sin i$, and fitting it to the RW Tri spectra. The continuum was removed from the RW Tri and template star spectra using a low order polynomial, after masking out strong absorption features. Each template was then artificially broadened in the velocity range $V_{rot} \sin i = 10 - 200$km/s in steps of 10km/s, assuming partial limb darkening (linear limb darkening coefficient $= 0.5$, North *et al.* 2000). These broadened template spectra were then compared with the orbital velocity corrected RW Tri spectra on each night. Residual spectra were produced by subtracting a constant times the shifted broadened template from each RW Tri spectrum; the constant was adjusted to minimise the scatter on each residual spectrum. A boxcar average smoothing was applied to the residual spectrum to eliminate any large scale structure. The reduced chi-squared (χ^2_ν) was calculated between each residual and smoothed spectrum in the wavelength regions containing the Na I absorption feature (22040Å to 22108Å) and the Ca I absorption feature (22614Å to 22689Å). The average results can be seen in Figure 8 where we plot night 1 and night 2 separately, and also combined.

The best fit (minimum χ^2_ν) for night 1 and 2 is obtained with $V_{rot} \sin i \sim 90$km/s and $V_{rot} \sin i \sim 140$km/s respectively (Figure 8). Based on the χ^2_ν distribution in Figure 8, we estimate a mean $V_{rot} \sin i = 120 \pm 20$km/s. All template stars gave the same order of Chi-squared values, confirming again that the data are not template sensitive in this wavelength band. The minimum χ^2_ν values had a range over all the templates of $V_{rot} \sin i$ from $80 - 100$km/s for night 1, and $130 - 150$km/s for night 2. We confirmed that the intrinsic $V_{rot} \sin i$ of each template was consistent with 0km/s, by cross correlating the templates against each other.

The analysis of the orbital radial velocity was not changed significantly when we broadened the template lines by 120km/s. This is because rotational broadening affects the profile of the absorption lines, but not the position of the line centroids which govern the cross correlation peak positions.

4 DISCUSSION

To calculate the masses of the two component stars in the system we can use the mass ratio (q),

$$q = \frac{K_1}{K_2} = \frac{M_2}{M_1}, \tag{2}$$

where K_1 and K_2 are the radial velocity amplitudes of the primary and secondary stars respectively, and M_1 and M_2 are the primary and secondary masses respectively.

4.1 Primary Star Velocity Measurements

There have been a number of different estimates of K_1 based on measurements of the optical emission lines in RW Tri and these have yielded a range of values. Doppler maps of RW Tri (Kaitchuck *et al.* 1983) indicate that the He II λ4686Å emission arises from the inner accretion disc region, He I λ4471Å emission is found further out in the accretion disc, and Hβ and Hγ emission originates from the outer regions of the accretion disc and the inner face of the secondary star.

Still *et al.* (1995) measured the emission line centroids and obtained K_1 values of 208 ± 8 km/s from Hβ, 223 ± 11 km/s from Hα, and 216 ± 9 km/s from He II (λ4686Å). The He II measurement of Still *et al.* (1995) is consistent with the 197$\pm$20 km/s measured by Kaitchuck *et al.* (1983), who also found a K_1 velocity of $\sim 170 \pm 20$ km/s for He I. Still *et al.* (1995) also used the convolution technique of Schneider & Young (1980) to measure the wings of the Hβ, Hγ and He II emission lines. The line wings, which come from high velocity gas in the inner disk, are in principle more likely to reflect the motion of the white dwarf than the line cores. The latter may well be contaminated by emission from the secondary star, the accretion stream, and the bright spot. However, Still *et al.* found that the measured velocities for the emission line wings in RW Tri were inconsistent with the velocities obtained from Doppler maps. These inconsistencies could be due to absorption affecting the wings of the accretion disc emission lines.

Recently HST data have been used to measure the velocity of narrow absorption features in the UV. Mason *et al.* (in prep.) detected velocity shifts in the UV absorption lines and found they had the same orbital phase as that expected for the white dwarf. The lines appear to originate in a layer above the inner accretion disk, and their motion may therefore mirror that of the white dwarf. By cross correlating the average spectrum through the orbital cycle they find $K_1 = 296 \pm 5$ km/s.

4.2 Effects on the Secondary Star Radial Velocity Amplitude

The apparent value of K_2 may be modified by heating, line-quenching, and line contamination (Friend *et al.* 1990). *Heating* of the secondary star occurs due to hard photons from the accretion disc. *Line quenching* occurs due to the ionisation of the absorption lines by flux from the disc. Both irradiation and line quenching can deplete the absorption line strength on the surface of the secondary star that faces the accretion disc, and shift the apparent centroid of the absorption line region to the hemisphere facing away from the disc. This would lead to an over estimate of the K_2 value. The magnitude of this effect may be reduced however if the accretion disk has a thick rim which shields the secondary. This appears to be the case in RW Tri (Mason, Drew & Knigge 1997). *Line contamination* may occur due to weak disc features. This could lead to variations in the line strengths of the absorption through the orbit.

To account for these effects, Wade & Horne (1988) estimated the likely correction required for the radial velocity amplitude of the secondary star. This "K-correction" is given by,

$$\Delta K = \frac{\Delta R}{a_2} K_2 = \frac{f R_2}{a_2} K_2, \tag{3}$$

where ΔR is the displacement between the effective centre and the centre of mass of the secondary star, R_2 is the secondary star radius, $|f| < 1$ is a weighting factor representing the strength of the absorption feature, and a_2 is the distance of the centre of mass of the secondary star from the centre of mass of the system given by,

$$a_2 = \frac{a}{1+q}, \tag{4}$$

where a is the separation of the component stars and q is the mass ratio ($q = M_2/M_1$).

To estimate the K correction, we use $f = 4/5\pi \sim 0.25$ where the front hemisphere of the secondary star has ~ 0.4 of the absorption of the back hemisphere. This is based on the measured change in the amplitude of the absorption features with orbital phase (Section 3.4). Each hemisphere is assumed to have uniform absorption, and we relate R_2/a to the mass ratio q using

$$\frac{R_2}{a} = \frac{0.49 q^{2/3}}{0.6 q^{2/3} + \ln(1 + q^{1/3})} \tag{5}$$

(Eggleton, 1983).

4.3 Mass Ratio Theory

Consider the conservative mass transfer equation,

$$\frac{\dot{R}_L}{R_L} = \frac{2\dot{J}}{J} + \frac{2(-\dot{M}_2)}{M_2}\left(\frac{5}{6} - q\right), \tag{6}$$

where R_L is the radius of the Roche Lobe, J is the orbital angular momentum, and -$\dot{M}_2$ is the instantaneous mass transfer rate (Frank, King & Raine 1992).

When $q(= M_2/M_1) < 5/6$ then $\dot{R}_L > 0$, so the Roche lobe expands, reducing the mass transfer, and the system is stable. In order to sustain long lived mass transfer the secondary star must expand in size relative to the Roche lobe, otherwise the lobes detach from the star and mass transfer stops. Evolution of the secondary star is one possibility, but for the secondary to evolve within the age of the Galaxy, it must be spectral type G0 or earlier (Patterson 1984). Most CV secondaries have spectral types later than G0, so a more likely solution for stable mass transfer is angular momentum loss due to either gravitational radiation and/or magnetic braking. The loss of angular momentum shrinks the binary system therefore enabling sustained mass transfer to occur.

When $q > 5/6$ then $\dot{R}_L < 0$, and the Roche lobe shrinks. Mass transfer will therefore increase, and the system will become unstable unless the secondary star can contract rapidly enough to keep its radius smaller than the radius of the Roche lobe. If the secondary star obeys the main sequence mass-radius relation $R_2 \propto M_2$, and the radius of the star responds to changes in its mass on a thermal time scale, Equation 6 becomes,

$$-\frac{\dot{J}}{J} = -\frac{\dot{M}_2}{M_2}\left(\frac{4}{3} - q\right), \tag{7}$$

yielding a critical upper mass ratio (q_{crit}). When $q > 4/3$ the secondary star will not shrink rapidly enough to keep pace with the Roche lobe. There will be a spontaneous overflow and mass transfer becomes unstable.

Table 4. Mass ratio results using our best estimate of the secondary star velocity, with a combination of white dwarf velocities.

Feature	K_1 (km/s)	K_2 (km/s)	q using K_2	q using $\Delta K \sim 24\%$
UV	296 ± 5	221 ± 29	1.34 ± 0.18	1.66 ± 0.27
Hα	223 ± 11	221 ± 29	1.01 ± 0.14	1.25 ± 0.21
He II	216 ± 9	221 ± 29	0.98 ± 0.14	1.21 ± 0.20
Hβ	208 ± 8	221 ± 29	0.94 ± 0.13	1.17 ± 0.20
He I	170 ± 20	221 ± 29	0.77 ± 0.14	0.96 ± 0.19

The secondary star in a CV is a late type low mass star with a deep convective envelope, and therefore loses mass on a dynamical time scale governed by the star's adiabatic response. Considering a complete polytrope with a polytropic index of $n = 3/2$ (Hjellming & Webbink 1987), the mass-radius relation for the secondary star becomes $R_2 \propto M_2^{-1/3}$, and hence Equation 6 becomes,

$$-\frac{\dot{J}}{J} = -\frac{\dot{M}_2}{M_2}\left(\frac{2}{3} - q\right), \tag{8}$$

producing a lower mass ratio limit ($q_{ad,fc}$). When $q > 2/3$ the star can not remain within its Roche lobe in hydrostatic equilibrium, and mass transfer occurs on dynamical time scales. When $q < 2/3$, the star becomes stable on a dynamical time scale and mass transfer occurs due to the slow expansion of the star via nuclear evolution or angular momentum loss causing the Roche lobe to contract.

The secondary star in RW Tri may not be fully convective so the true adiabatic mass ratio will be higher. In the case where the secondary star has a convective envelope, but a radiative core, the mass-radius relation becomes $R_2 \propto M_2^{1/3}$, leading to a mass ratio of $q_{ad,rc} = 1$ for the adiabatic response (Hjellming & Webbink 1987).

4.4 Mass Ratio

We first calculate the mass ratio of RW Tri using the various estimates of the component star radial velocity amplitudes. The most reliable estimate for the secondary star velocity is from the K-band data because there is not enough detail in the I-band data to be sure that they are not affected by telluric lines and background emission etc. When combined with the K-band secondary star velocity (221 ± 29km/s), the various estimates of the primary star velocity amplitude discussed in Section 4.1 lead to a range of mass ratios of $0.8 - 1.3$ as expressed in Table 4 (column 4).

The K_1 velocity values that *a priori* are most likely to reflect the motion of the white dwarf are the UV absorption lines of Mason *et al.* (2002), and the He II emission lines of Still *et al.* (1995), because they both originate in regions close to the white dwarf. These velocities therefore give us a 'most likely' mass ratio in the range $1.0 - 1.3$. To consider the effects of the "K-correction" on our most likely mass ratio range, we use Equation 3 and 5, and $f \sim 0.25$ with $q = 1.0 - 1.3$, which corresponds to a range in ΔK of $\sim 19\%$ to $\sim 24\%$. Thus after applying the most likely value for the secondary star heating the value of K_2 in RW Tri is ~ 178km/s, implying a revised mass ratio, q, in the range $1.2 - 1.7$ (Table 4, column 5).

Alternatively we can calculate the mass ratio of RW Tri

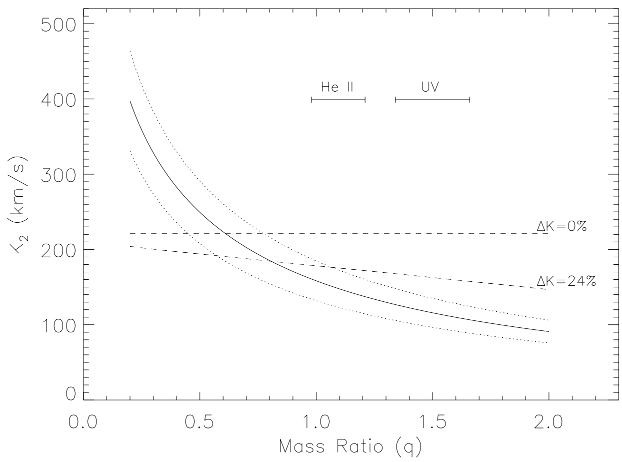

Figure 9. Radial velocity of the secondary star (K_2) versus a range of mass ratios ($q = M_2/M_1$). The solid curved line represents K_2 calculated using $V_{rot} \sin i = 120$km/s, and Equations 9 and 5. The dotted curved lines represent K_2 using $V_{rot} \sin i = 120 \pm 20$km/s. The dashed straight lines represent the variation of K-corrected $K_2 = 221$km/s (Section 4.2)as a function of mass ratios, when $\Delta K = 0\%$ and $\Delta K = 24\%$. The horizontal bars labeled He II and UV represent the mass ratio range of He II and UV respectively, using $\Delta K = 0\%$ and $\Delta K = 24\%$ from Table 4.

using the rotational broadening of the secondary star, independent of K_1. Assuming that the secondary star rotates in phase with the binary orbit we use,

$$\frac{K_2}{V_{rot} \sin i} = \left[(1+q)\left(\frac{R_2}{a}\right)\right]^{-1} \tag{9}$$

where R_2/a is found using Equation 5. The results are shown in Figure 9 where the solid line represents the K_2 values implied by $V_{rot} \sin i = 120$km/s (from Section 3.6) as a function of mass ratio between $q = 0.2$ and $q = 2.0$. The dotted lines show the effects of changing $V_{rot} \sin i$ by ± 20km/s. The dashed lines in Figure 9 represent the K-corrected secondary star velocity as a function of the mass ratio, for the cases $\Delta K = 0\%$ and $\Delta K = 24\%$. We find a self-consistent value of q in the range $0.5 - 0.8$ when no correction for possible heating effects is applied ($\Delta K = 0\%$). This does not agree with the mass ratio range derived for either He II or UV K_1 velocities, which are indicated in Figure 9. When $\Delta K = 24\%$, the allowed mass ratio range is $q = 0.6 - 1.1$ (Figure 9), and again does not overlap with either the He II or UV range.

This can be more clearly seen in Figure 10 where the derived values of q are expressed as a function of ΔK. The solid black line in Figure 10 shows the mass ratio at which the K_2 value implied by $V_{rot} \sin i = 120$ km/s equals the K-corrected value of K_2 (adopting an observed value of K_2 of 221 km/s). Again the dotted lines indicate the effect of changing $V_{rot} \sin i$ by ± 20 km/s. The dashed and thick solid lines represent the mass ratio derived using the He II and UV line estimates of K_1 in combination with the K-corrected value of K_2, as a function of ΔK. Figure 10 shows that $V_{rot} \sin i$ is consistent with the He II-based mass ratio range only for $\Delta K > 34\%$, and higher still for the UV-based K_1 value (cf. our best estimate of $\Delta K \sim 24\%$). This is greater than the we find in Section 4.2, suggesting that velocities found using the UV and He II emission lines may contain non-orbital components.

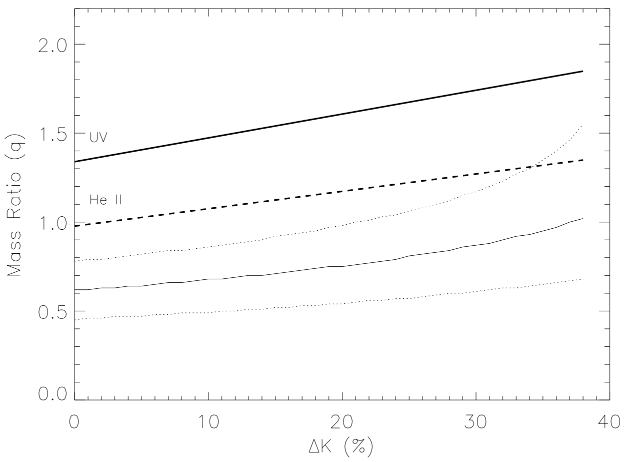

Figure 10. The possible mass ratio ranges of RW Tri ($q = M_2/M_1$) as a function of the "K-correction" of the secondary star (ΔK) due to heating effects. The solid black curved line represents the mass ratio (q) found when a K_2 using $V_{rot} \sin i$ = 120km/s (solid black curved line in Figure 9) coincides with a K-corrected K_2 = 221km/s (dashed lines in Figure 9), as a function of ΔK. The dotted curved lines represent the mass ratio as a function of ΔK using $V_{rot} \sin i = 120 \pm 20$km/s. The thick solid and thick dashed lines represent the mass ratio range of He II and UV respectively, as a function of ΔK using Equation 3.

4.5 Masses

Using the Roche Lobe geometry, a relationship between the mass ratio (q), orbital inclination angle (i) and eclipse duration was derived by Chanan *et al.* (1976) and also by Horne (1993). Because the temperature of the accretion disk increases towards its centre, the UV emission of the disk will be more concentrated around the white dwarf than the optical emission. Thus an eclipse width at half light measured in the UV is likely to be a better approximation to the white dwarf eclipse duration than one measured in the optical band. Using the relationships of Chanan *et al.* (1976) and Horne (1993), the mass ratio, and the eclipse width at half light of 0.077 ± 0.002 from the UV light curves of Mason *et al.* (1997), a set of inclination angles can be calculated. These inclination angles range from 73^o to 79^o for mass ratios between 0.5 and 1.1. Hence a range of masses for the primary and secondary stars can be derived using,

$$M_1 \sin^3 i = \frac{P_{orb} K_2}{2\pi G}[K_1 + K_2]^2, \quad (10)$$

and,

$$M_2 \sin^3 i = \frac{P_{orb} K_1}{2\pi G}[K_1 + K_2]^2. \quad (11)$$

The results derived using the UV and He II K_1 velocities are shown in Figure 11. Using the UV measurement, both the uncorrected and K-corrected mass ratios lie above the critical value of 4/3 (Section 4.3), in the region of the diagram where mass transfer is unstable. The upper mass for the primary star exceeds the Chandrasekhar mass limit of $1.44M_\odot$, and the secondary star mass is also very large and inconsistent with that of a main sequence star. This reinforces our suspicions that the UV velocities contain a non-orbital component. A reduction of K_2 below the K-corrected value of 178km/s would decrease the secondary mass, but further increase the mass ratio.

Adopting instead the K_1 measurement derived from He II data, we find values of q that broadly lie between $q_{crit} = 4/3$ and $q_{ad,rc} = 1$. The masses for the primary and secondary stars lie in the range of $0.8 - 1.1M_\odot$, and $0.9{-}1.1M_\odot$ respectively. The white dwarf mass is well within the Chandrasekhar mass limit of $1.44M_\odot$, and includes the mean primary mass of $0.8M_\odot$ for CV systems with $P_{orb} > 3$ hrs (Smith & Dhillon 1998b). The lower limit for the secondary star mass, however, exceeds the predicted mass of $0.55M_\odot$ based on the main sequence mass-radius relation for an orbital period of 5.25 hours (Echevarría 1983).

Given the evidence for a non-orbital component in the UV absorption line velocities, we cannot be certain that the optical emission line velocities are not similarly affected. If we force the secondary star mass to its equivalent main sequence value, $0.55M_\odot$, we would predict a primary star velocity of $152 - 169$km/s for $K_2 = 221 - 178$km/s. This is closer to the K_1 value of 170 ± 20km/s derived by Kaitchuck *et al.* (1983) from the He I emission line. The implied mass ratio for a K_1 velocity of 170km/s is in the range 0.8 ($\Delta K = 0\%$) to 1.0 ($\Delta K = 24\%$), and is consistent with the rotational velocity of the secondary that we derive (Figure 10).

Alternatively, we can obtain mass values using the combination of $V_{rot} \sin i$ and K_2 without any assumptions about K_1. Using the mass ratio values of $0.6 - 1.1$ for $\Delta K = 24\%$, and $0.5 - 0.8$ for $\Delta K = 0\%$ from Section 4.4, and assuming K_2 values of 178km/s and 221km/s respectively, the stellar masses can be calculated using Equations 2, 10, and 11. Figure 11 shows the results. The most likely mass of the primary and secondary stars lies between $0.4 - 0.7M_\odot$ and $0.3 - 0.4M_\odot$ respectively for the range of $\Delta K = 24 - 0\%$, and better agree with the expected masses for the component stars in a CV. The expected value of K_1 based on these results is in the range 120-130 km/s, with an upper limit of approximately 190 km/s.

5 CONCLUSIONS

I-band observations of RW Tri yield a secondary star radial velocity amplitude of 250 ± 47 km/s using the skew mapping technique. K-band observations of RW Tri provide us with a secondary star velocity of 221 ± 29 km/s which is obtained directly from the observations without using complex mapping methods. The two velocities are consistent within the errors.

We estimate the rotational velocity of the secondary star to be 120 ± 20km/s using the K-band UKIRT observations. Combining this velocity with the secondary star radial velocity corrected for non-uniform heating derived from the variation in the absorption line strengths, we find a mass ratio range of $0.6 - 1.1$, which contains the lower adiabatic response limit ($q_{ad,fc} = 2/3$). The uncorrected radial velocity results lead to a mass ratio range of $0.5 - 0.8$.

Combining the radial velocity amplitudes of the secondary star with the radial velocity of the primary determined from He II emission lines in the optical (Still *et al.* 1995) and narrow absorption lines in the UV (Mason *et al.* in prep.), yields a range of mass ratios of $1.0 - 1.3$ and $1.2 - 1.7$

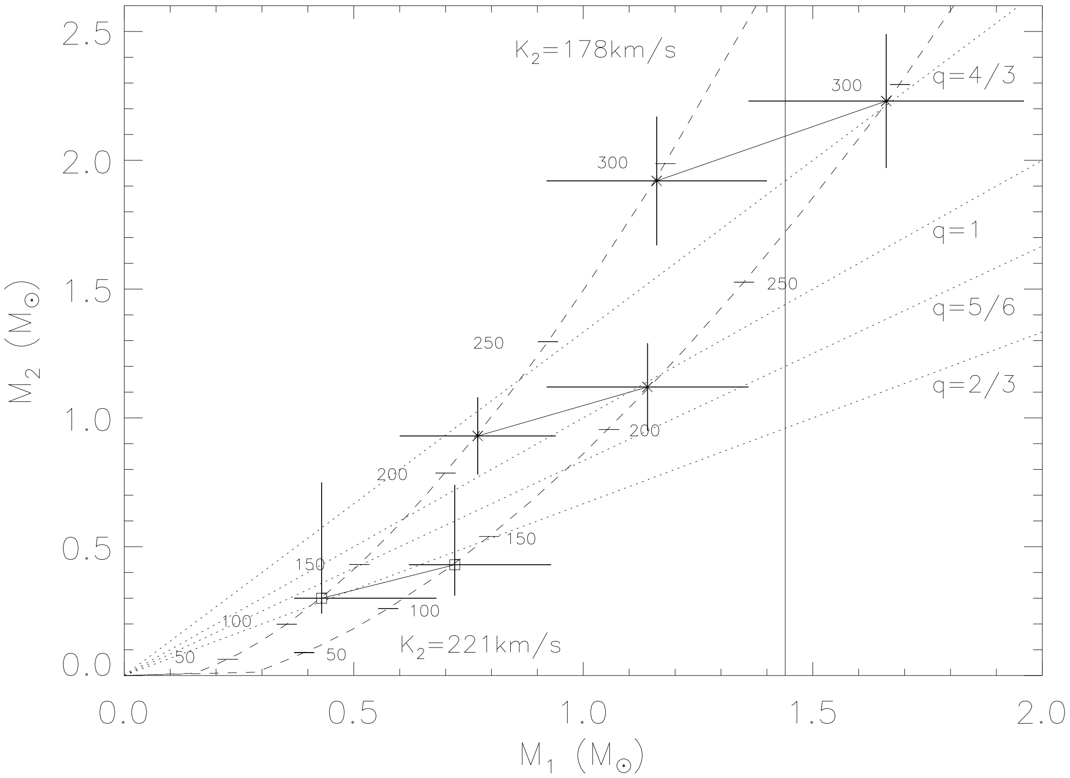

Figure 11. The mass of the component stars in RW Tri, derived by combining the measurement of K_2 with different estimates of K_1 (represented as $*$) , and from the combination of K_2 with $V_{rot} sini$ (represented by $\Box$). In each case we show values corrected for the effects of heating of the secondary using $\Delta K \sim 24\%$ ($K_2 = 178$ km/s - Section 4.3) and also with no heating correction ($K_2 = 221$ km/s), linked by a straight line. The upper set of results are obtained using the UV absorption $K_1 = 296 \pm 5$ km/s velocity (Mason *et al.* in prep), and the middle set of results are obtained using the He II accretion disc emission $K_1 = 216 \pm 9$ velocity (Still *et al.* 1995). The error bars combine the uncertainties in K_1 and K_2. The lower set of results show the mass values derived from the K_2 measurement combined with $V_{rot} \sin i = 120 \pm 20$km/s. The error bars are calculated using the ± 20km/s uncertainty on $V_{rot} \sin i$. The vertical solid line represents the $1.44 M_{\odot}$ Chandrasekhar mass limit for white dwarf stars. The two dashed lines represent the locus of masses calculated when $K_2 = 221$km/s and $K_2 = 178$km/s respectively with varying K_1 values; the tick marks on the two dashed lines mark K_1 velocity values of 50km/s, 100km/s, 150km/s, 200km/s, 250km/s and 300km/s. The four dotted lines represent the $q_{crit} = 4/3$ thermal mass transfer limit, $q_{ad,rc} = 1$ adiabatic response with a radiative core, $q = 5/6$ and $q_{ad,fc} = 2/3$ fully convective lower adiabatic response limit respectively (Section 4.2).

respectively, based on a range in the secondary heating correction of $\Delta K = 0 - 24\%$. The UV mass ratio range lies above the critical mass ratio ($q_{crit} = 4/3$); this range is also inconsistent with the rotational velocity results, indicating that the UV velocity very likely includes a non-orbital component. The He II mass ratio range lies between $q_{crit} = 4/3$ and q=5/6, but is only marginally consistent with the measured secondary rotational velocity, and may also contain a non-orbital component. By combining the data on the rotational broadening of the secondary with its measured orbital velocity, with no assumptions regarding the white dwarf velocity, we find most likely values of the primary and secondary masses that lie in the range $0.4 - 0.7 M_{\odot}$ and $0.3 - 0.4 M_{\odot}$ respectively, depending on the degree of secondary star heating. The most likely value of K_1 is predicted to be 120-130 km/s.

ACKNOWLEDGMENTS

We thank Paul Hirst for help with CGS4 data reduction. The United Kingdom Infra-Red Telescope is operated by the Joint Astronomy Centre on behalf of the U.K. Particle Physics and Astronomy Research Council. Also thanks to Dave Vande Putte for valuable discussion on the INT data, and Tom Marsh for use of, and help with, MOLLY. In our research, we have used, and acknowledge with thanks, data from the AAVSO International Data base, based on observations submitted to the AAVSO by variable star observers worldwide. We would also like to thank the referee for a careful reading of the manuscript and useful comments.

REFERENCES

Chanan, G. A., Middleditch, J., & Nelson, J. E., 1976, ApJ, 208, 512

Dhillon, V. S., Littlefair, S. P., Howell, S. B., Ciardi, D. R., Harrop-Allin, M. K., & Marsh, T. R., 2000, MNRAS, 314, 826

Echevarría, J., 1983, Rev. Mexicana Astron. Astrof., 8, 109

Eggleton, P. P., 1983, ApJ, 268, 386

Frank, J., King, A., & Raine, D., 1992, Accretion Power in Astrophysics, Cambridge University Press

Friend, M. T., Martin, J. S., Smith, R. C., & Jones, D. H. P., 1990, MNRAS, 246, 637

Friend, M. T., Martin, J.S., Smith, R. C., & Jones, D. H. P., 1988 MNRAS, 233, 451
Hjellming, M. S, & Webbink, R. F., 1987, ApJ, 318, 754
Horne, K., 1993, Accretion Discs in Compact Stellar Systems, 117, edited C. Wheeler.
Kaitchuck, R. H., Honeycutt, R. K., & Schlegel, E. M., 1983, ApJ, 267, 239
Marsh, T. R., White II, J. C., & Mansperger, C. A., 1994, ApJS, 93, 519
Martin, J.S., 1988, DPhil thesis, University of Sussex
Mason, K., O., *et al.* 2002 MNRAS, in preparation
Mason,K., O., Drew, J. E., & Knigge, C., 1997, MNRAS, 290, L23
North, R. C., Marsh, T. R., Moran, C. K. J., Kolb, U., Smith, R. C., & Stehle, R., 2000, MNRAS, 313, 383
Patterson, J., 1984, ApJS, 54, 443
Protitch, M., 1937, Bull. Astr. Obs. Belgrade, 38, 9
Robinson, E. L., Shetrone, D., & Africano, J. L., 1991, AJ, 102, 1176
Schneider, D. P., Young, P, 1980, ApJ, 240, 871
Smith, D. A., Dhillon, V. S., & Marsh, T. R., 1998a MNRAS, 296, 465
Smith, D. A.,& Dhillon, V. S., 1998b, MNRAS, 301, 767
Smith, R. C., Cameron, A. C., & Tucknott, D. S., 1993, in Regev O., Shaviv G., eds, Cataclysmic Variables and Related Physics. Inst. Phys. Publ., Bristol, p. 70
Still, M. D., Dhillon, V. S., & Jones, D. H. P., 1995, MNRAS, 273, 849
Vande Putte, D., Smith, R. C., Hawkins, N. A., & Martin, J. S., 2002, MNRAS, submitted
Wade, R., A., & Horne K., 1988, ApJ, 324, 411